Science Advances
AAAS

advances.sciencemag.org/cgi/content/full/5/2/eaav2111/DC1

Supplementary Materials for

Strictures of a microchannel impose fierce competition to select for highly motile sperm

Meisam Zaferani, Gianpiero D. Palermo, Alireza Abbaspourrad*

*Corresponding author: alireza@cornell.edu

Published 13 February 2019, *Sci. Adv.* **5**, eaav2111 (2019)
DOI: 10.1126/sciadv.aav2111

The PDF file includes:

Other Supplementary Material for this manuscript includes the following:

(available at advances.sciencemag.org/cgi/content/full/5/2/eaav2111/DC1)

Supplementary Materials

Delta (δ) value

Sperm flagellum movement is not uniform. Instead, it has greater oscillation amplitude at the end of its tail in comparison to the head. This difference in oscillation amplitude at the end of the tail and the head leads to the tilted movement of the sperm in the withdrawal distance, and subsequently the tail experiences higher flow rate in comparison with the head (as the head is very close to the boundary). As a result, the shear rate close to each wall (sidewalls and top surface) plays the main role in sperm rheotaxis and the boundary swimming movement (Eq. 5). δ is a geometrical value used to describe this tilted orientation(16), as shown in the fig. S1. According to the δ value reported for sperm, the final orientation of the sperm during the boundary swimming movement is $\delta/_{L} \sim \frac{\pi}{20}$, in which L is the sperm length. The tilted orientation of the sperm therefore makes it susceptible to the flow of the sperm medium.

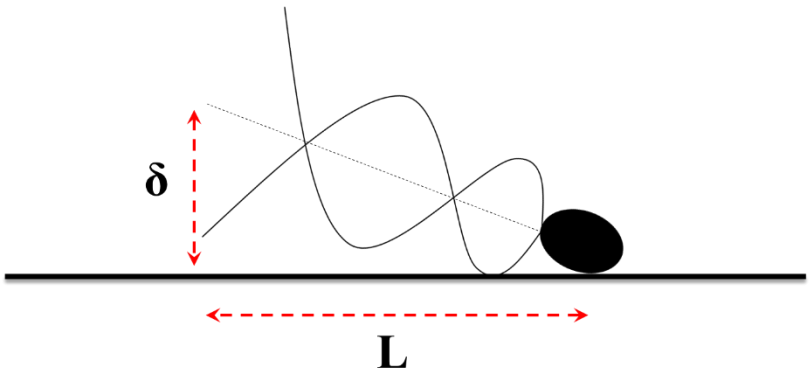

Fig. S1. Sperm tilted orientation in the boundary swimming mode.

Lubrication approximation

At distances closer than 50 μm to the sidewalls, the far-field approximation is not accurate. To simulate the imposed drift velocity and subsequent rotations at near-wall conditions, we used lubrication theory (*35*). To apply the lubrication theory, we modeled the problem of a sperm approaching a wall with an incidence angle of $\frac{\pi}{2} - \theta$ and translational velocity of V, by a thin rectangular body with the same translational velocity and orientation, as depicted in fig. S2.

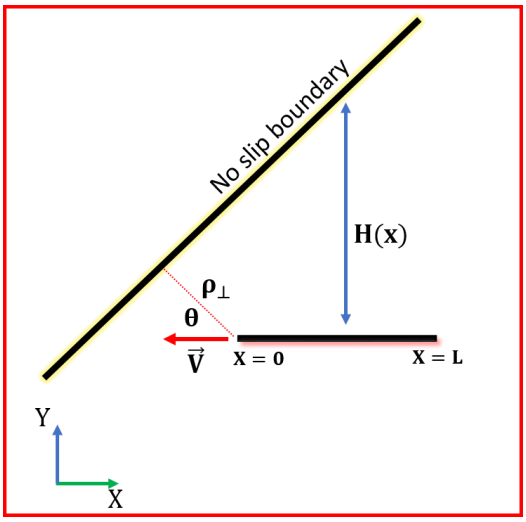

Fig. S2. Schematic of the model used for lubrication theory.

Based on the model, the boundary conditions can be written as

$$v_x = v_y = 0 \text{ at } y = H(x) \quad \text{(S1)}$$

$$H(x) = H_0 + x\cot(\theta) \quad \text{(S2)}$$

$$v_x = -V \text{ and } v_y = 0 \text{ at } y = 0 \quad \text{(S3)}$$

$$p = p_0 \text{ at } x = 0 \text{ and } L \quad \text{(S4)}$$

Using these boundary conditions, and solving the Stokes equation in the $\hat{y}$ direction using lubrication theory, the pressure distribution between the sperm and the sidewall can be described by

$$p = \frac{V\mu}{2\cot(\theta)}\left(\frac{1}{H(0)+x\cot(\theta)} - \frac{1}{H(0)} - \frac{H(0)H(L)\cot(\theta)L}{(H(L)^2-H(0)^2)(H(0)+x\cot(\theta))^2} + \frac{H(0)H(L)\cot(\theta)L}{(H(L)^2-H(0)^2)H(0)^2}\right) + p_0 \qquad (S5)$$

in which $H(0)$ and x are functions of time (i.e., sperm velocity changes these values over time). Subsequently, the repulsive force imposed on the sperm by the presence of the sidewall can be written as:

$$F_L = \int_0^L (p - p_0)dx = \frac{6\mu V}{\cot^2(\theta)}\left(\frac{2L\cot(\theta)}{2H(0)+L\cot(\theta)} + \ln\left(\frac{H(0)}{H(0)+L\cot(\theta)}\right)\right) \qquad (S6)$$

Based on the repulsive force obtained from the lubrication approximation, we obtained the time derivate of $H(x)$ to be

$$\frac{dH(x)}{dt} = \frac{d}{L\xi_\perp}F_L \qquad (S7)$$

In this part, we only considered the effect of lubrication as near wall hydrodynamic interactions, and the change of $H(x)$ due to sperm velocity is considered in Eq. 1 of the main manuscript.

Moreover, the forces imposed on the anterior half of the sperm ($0 \le x \le \frac{L}{2}$) and posterior half of the sperm ($\frac{L}{2} \le x \le L$) are not equal as they can be calculated by

$$F_L = \int_0^{L/2}(p - p_0)dx = \frac{6\mu V}{\cot^2(\theta)}\left(\frac{2L\cot(\theta)}{4H(0)+L\cot(\theta)} + \ln\left(\frac{2H(0)}{2H(0)+L\cot(\theta)}\right)\right) \quad (S8)$$

$$F_R = \int_{L/2}^{L}(p - p_0)dx = \frac{6\mu V}{\cot^2(\theta)}\left(\frac{2L\cot(\theta)}{4H\left(\frac{L}{2}\right)+L\cot(\theta)} + \ln\left(\frac{2H\left(\frac{L}{2}\right)}{2H\left(\frac{L}{2}\right)+L\cot(\theta)}\right)\right) \quad (S9)$$

The imbalance between forces imposed on the anterior and posterior halves of the sperm indicates a rotation in the swimmer. To find the rotation induced on the sperm by the presence of the sidewall, we first obtained the torque imposed by the pressure distribution

$$T_1 = \int_0^L (p(x) - p_0)\left(x - \frac{L}{2}\right)dx \quad (S10)$$

$$= \frac{V\mu}{2\cot(\theta)}\left[\tan^2(\theta)\left(\tilde{H} + \frac{\tilde{H}H_L}{2\tilde{H}-4H_0}\right)\ln\left(\frac{H_0}{H_0+L\cot(\theta)}\right) + \frac{H_L\tan^3(\theta)}{2-\frac{4H_0}{\tilde{H}}}\left(\frac{1}{H_0} - \frac{1}{H_0+L}\right) + L\tan\theta)\right] \quad (S11)$$

where H_0, $\widetilde{H}$, and H_L are $H(0)$, $H(L/2)$, and $H(L)$, respectively. The general torque produced by the drag force can be written out as

$$T_2 = \int_0^L \left(x - \frac{L}{2}\right) \Omega_{HI} \left(x - \frac{L}{2}\right) \xi_\perp dx = \frac{L^3 \Omega_{HI} \xi_\perp}{12} \quad \text{(S12)}$$

Since the sperm is an autonomous microswimmer, the torque-free condition ($T_1 + T_2 = 0$) is required. Hence, the rotation induced by the sidewall is obtained as

$$\Omega_{HI} = \frac{6V\mu d}{L^3 \xi_\perp \cot(\theta)} \left[\tan^2(\theta) \left(\widetilde{H} + \frac{\widetilde{H} H_L}{2\widetilde{H} - 4H_0} \right) \ln\left(\frac{H_0}{H_0 + L\cot(\theta)} \right) + \frac{H_L \tan^3(\theta)}{2 - \frac{4H_0}{\widetilde{H}}} \left(\frac{1}{H_0} - \frac{1}{H_0 + L} \right) + L \tan\theta \right) \right] \quad \text{(S13)}$$

where d is the sperm width and considered to be 5μm.

Intrinsic angular velocity of sperm

Intrinsic angular velocity

To derive the angular velocity of a sperm imposed by its periodic flagellum movement, we assumed that flagellum shape over time is a sum of simple sine waves(*36*, *37*) with the amplitudes of y_i, temporal frequencies of ω_i, and phases of ϕ_i. For simplicity, we assumed that all the sine waves were moving with an identical wave number k

$$y(x,t) = \sum y_i \sin(kx - \omega_i t + \phi_i) \quad \text{(S14)}$$

Therefore, the vertical component of the velocity of a segment of the flagellum is the time-derivative of $y(x,t)$, whereas the horizontal component of the velocity is zero (Eq. S15). Also, to apply resistive force theory and derive the expression for sperm movement, its velocity was decomposed into tangential and normal components

$$\vec{V} = \left(0, \frac{\partial y}{\partial t}\right) \tag{S15}$$

To decompose this velocity into tangential and normal components, the tangent and normal unit vectors (Eq. S16 & 17) must be plugged into Eq. S18, which is a standard notion of force-velocity relation in established resistive force theory(*37*, *38*), in which ξ_n and ξ_t are anisotropic friction coefficients of the normal and tangential directions, respectively

$$\hat{e}_t = \frac{1}{\sqrt{1+\left(\frac{\partial y}{\partial x}\right)^2}}\left(1, \frac{\partial y}{\partial x}\right) \approx \left(1 - \frac{1}{2}\left(\frac{\partial y}{\partial x}\right)^2\right)\left(1, \frac{\partial y}{\partial x}\right) \tag{S16}$$

$$\hat{e}_n = \frac{1}{\sqrt{1+\left(\frac{\partial y}{\partial x}\right)^2}}\left(-\frac{\partial y}{\partial x}, 1\right) \approx \left(1 - \frac{1}{2}\left(\frac{\partial y}{\partial x}\right)^2\right)\left(-\frac{\partial y}{\partial x}, 1\right) \tag{S17}$$

$$\vec{f} = -\xi_t\left(\vec{V}.\hat{e}_t\right)\hat{e}_t - \xi_n\left(\vec{V}.\hat{e}_n\right)\hat{e}_n \tag{S18}$$

Using the small amplitude approximation, the propulsive force generated by the sperm flagellum at a given x and t is described by Eq. S19

$$f_x \approx (\xi_n - \xi_t)\frac{\partial y}{\partial t}\frac{\partial y}{\partial x} \tag{S19}$$

The total force in the horizontal direction ($\hat{x}$) must be calculated by integrating the force over the entire flagellum in one period (Eq. S20)

$$\langle f_x \rangle \approx \frac{1}{LT}\int_0^T dt \int_0^L dx\, (\xi_n - \xi_t)\frac{\partial y}{\partial t}\frac{\partial y}{\partial x} \tag{S20}$$

By assuming that for $i > 1$, $y_i \ll y_1$, then Eq. S20 yields to Eq. S21

$$\langle f_x \rangle \approx -\frac{1}{2}(\xi_n - \xi_t){y_1}^2\omega_1 k \tag{S21}$$

and consequently, the propulsion velocity can be described by Eq. S22. As can be seen, the propulsion velocity is correlated to the amplitude, frequency, and vector number of the sine wave with the greatest amplitude

$$v_{propulsion} \approx -\frac{1}{2}\left(\frac{\xi_n}{\xi_t} - 1\right) {y_1}^2 \omega_1 k \tag{S22}$$

In addition to the velocity generated in the $\hat{x}$ direction, the general force generated in the $\hat{y}$ direction for a segment of the flagellum is described by Eq. S23

$$f_y \approx -\xi_n \frac{\partial y}{\partial t} + (\xi_n - \xi_t) \frac{\partial y}{\partial t} \left(\frac{\partial y}{\partial x}\right)^2 \tag{S23}$$

Likewise, the general force in the $\hat{y}$ direction is the integral of f_y over a period and the whole flagellum. Obviously, the first term of Eq. S23 vanishes after integration over the whole flagellum. Therefore, the generated force in the $\hat{y}$ direction is

$$\langle f_y \rangle \approx \frac{(\xi_n - \xi_t)}{LT} \int_0^T dt \int_0^L dx \, (-\sum y_i \omega_i \cos(kx - \omega_i t + \phi_i))(\sum y_i k \cos(kx - \omega_i t + \phi_i))^2. \tag{S4}$$

By assuming that the sperm flagellum is composed of two sine waves, Eq. S24 reduces to

$$\begin{aligned} \langle f_y \rangle \approx \frac{(\xi_n - \xi_t)}{LT} \int_0^T dt \int_0^L dx (&-{y_1}^2 y_n k^2 \cos(kx - \omega_n t + \phi_2) \cos^2(kx - \omega_1 t + \phi_1)(\omega_n + 2\omega_1) + \\ &-y_1 {y_n}^2 k^2 \cos(kx - \omega_1 t + \phi_1) \cos^2(kx - \omega_n t + \phi_2)(2\omega_n + \omega_1)) . \end{aligned} \tag{S25}$$

Therefore, by assuming that $y_1 \gg y_n$, Eq. S25 yields to

$$\langle f_y \rangle \approx -{y_1}^2 y_n k^2(\omega_n + 2\omega_1)(\xi_n - \xi_t)\frac{1}{LT}\left[\frac{\cos(2\phi_1 - \phi_n)}{4k(2\omega_1 - \omega_n)} + \frac{\cos(\phi_n)}{2\omega_n k} + \frac{\cos(2\phi_1 + \phi_n)}{12k(2\omega_1 + \omega_n)}\right]. \quad \text{(S26)}$$

In particular, if $\omega_n = n\omega_1$, $\phi_1 = 0$, and $\phi_n = \phi$, then Eq. S26 reduces to

$$\langle f_y \rangle \propto -{y_1}^2 y_2 k(\omega_n + 2\omega_1)(\xi_n - \xi_t)\cos(\phi). \quad \text{(S27)}$$

Eventually, by considering that $v_{rotation} = \frac{\langle f_y \rangle}{\xi_n}$ and $\Omega_{intrinsic} = \frac{v_{rotation}}{L}$, the $\Omega_{rotation}$ is(*39*):

$$\Omega_{IN} \propto -{y_1}^2 y_n \frac{\omega_n + 2\omega_1}{L^3}\left(1 - \frac{\xi_t}{\xi_n}\right)\cos(\phi). \quad \text{(S28)}$$

The final equation obtained for the intrinsic angular velocity shows that depending on ϕ, sperm movement can intrinsically have angular velocity, and therefore when the flow of the sperm medium is zero, the sperm trajectory can feature intrinsic curvature.

In the presence of fluid flow, as we clarified in the main text in Eq. 4, the angular velocity of the sperm is the sum of its intrinsic angular velocity and its rheotactic behavior as a response to external fluid flow(*21*). According to Eq. S28, the intrinsic angular velocity of sperm can be either constructive ($\phi = 0 \rightarrow \Omega_{IN} = -\Omega_{max}$) or destructive ($\phi = \pi \rightarrow \Omega_{IN} = \Omega_{max}$) to the

angular velocity imposed by the fluid flow. The impact of the intrinsic angular velocity on the trajectory of sperm is demonstrated in Fig. 1(g), which demonstrates the constructive effect of the intrinsic curvature leads to a decrease in the withdrawal distance. Moreover, the destructive effect of the intrinsic angular velocity is shown as well, leading to an increase in the withdrawal distance. As a result, the withdrawal distance can vary slightly depending on the ϕ. To perform these simulations, it was assumed that the sperm oscillation frequency is constant, and consequently by plugging Eq. S22 into Eq. S28, a linear relation between intrinsic angular velocity and propulsion velocity (Eq. S29) can be obtained:

$$\Omega_{IN} \propto v_{propulsion} \left(\frac{\xi_t}{\xi_n}\right) \frac{y_n}{L^2} \cos(\phi) \tag{S29}$$

Two important results from these calculations include: (1) the withdrawal distance of the sperm cell is not significantly influenced by the intrinsic angular velocity of the sperm, and the major part of the sperm rotational movement is due to sperm rheotaxis; (2) even if the intrinsic curvature is not assumed to be negligible, as is demonstrated in Fig. 1(g) and Eq. S29, the sperm with higher velocity have higher corresponding intrinsic rotations. This means that the intrinsic angular velocity maintains the sperm with higher velocities closer to each other below the stricture. That is, for two highly motile sperm, the sperm with higher velocity and a destructive intrinsic rotation and the sperm with lower velocity and the constructive intrinsic rotation are not distinct. Therefore, the intrinsic rotation of the sperm is consistent with the fierce competition phenomenon among highly motile sperm.

Experimental measurement of intrinsic angular velocity

To experimentally confirm the existence of the intrinsic angular velocity, we observed the sperm swimming when the flow of the sperm medium was zero (Movie S1). The sperm trajectory in this zone is depicted in fig. S3(a). Interestingly, most of the sperm (90%) in the zone with zero medium flow were rotating clockwise, and as can be seen in trajectories extracted for four different sperm (fig. S3(b)), the curvature of the sperm remained roughly constant over time. We measured the intrinsic angular velocity of 28 sperm with different velocities (fig. S4) and determined the mean value for their angular velocity was $0.12 \pm 0.06\ \mathrm{s}^{-1}$.

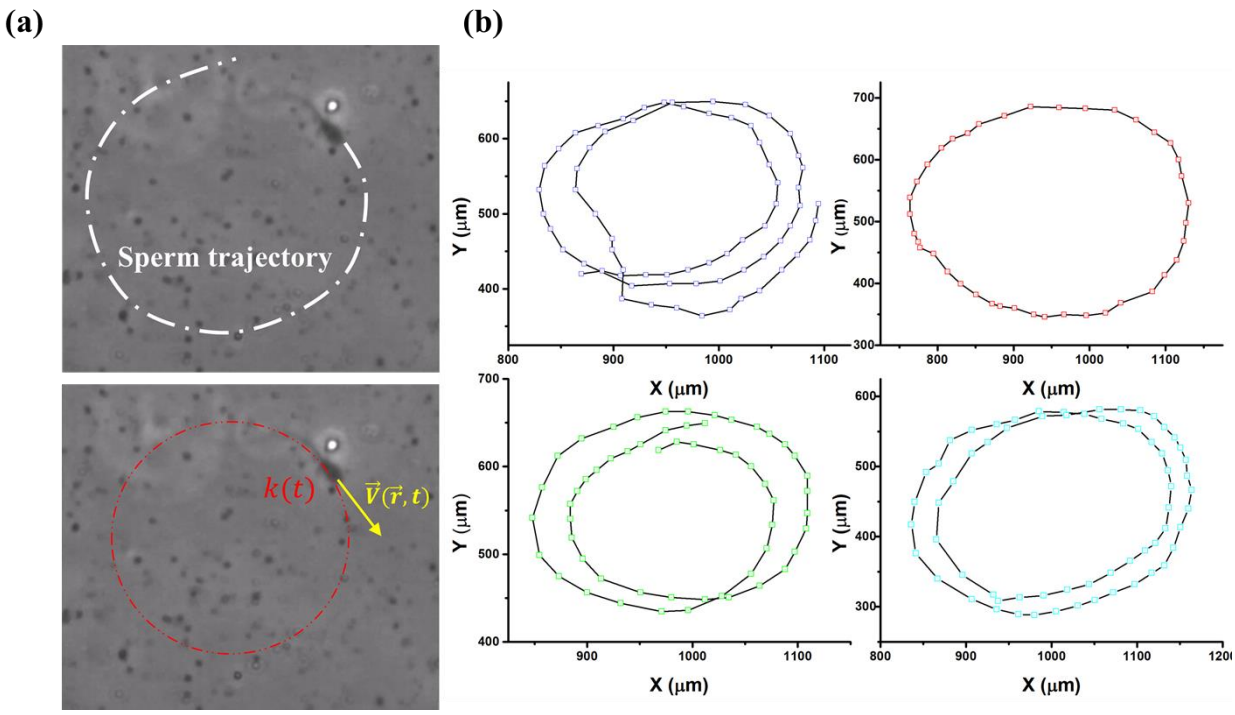

Fig. S3. Sperm intrinsic angular velocity and curvature. (a) Sperm pseudo-circular trajectory with a curvature of $k(t)$, which is roughly constant over time. (b) Trajectories of four different sperm in intrinsic rotation mode. The corresponding curvature of the trajectories were $8.24 \pm 1.24 \times 10^{-3}\mu m^{-1}$ (top-left), $12.4 \pm 2.32 \times 10^{-3}\mu m^{-1}$ (top-right), $8.08 \pm 0.94 \times 10^{-3}\mu m^{-1}$ (bottom-left), and $9.41 \pm 1.06 \times 10^{-3}\mu m^{-1}$ (bottom-right)

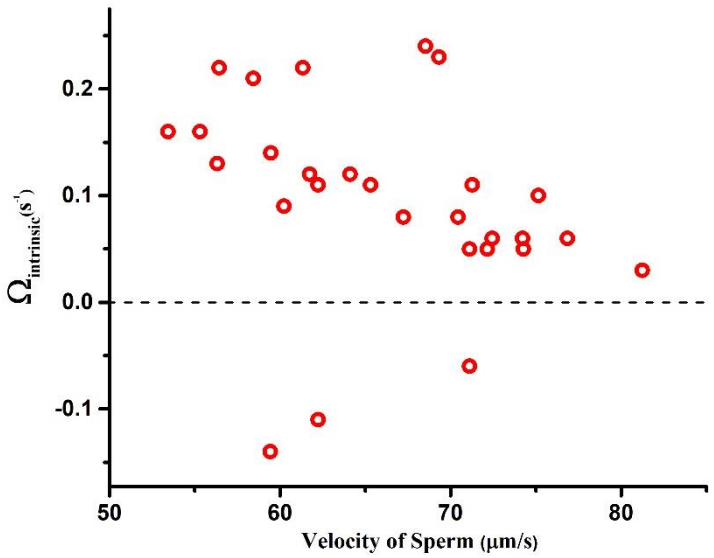

Fig. S4. Intrinsic angular velocities measured for sperm when the external flow was zero. Most of the sperm (~90%) swam in a clockwise direction ($\Omega_{IN} > 0$).

Impact of stricture mouth angle on sperm motion

The characteristics of the sperm butterfly-shaped motion highly depends on the stricture mouth angle, β. To demonstrate the impact of β on the sperm motion, the equations of motion were solved for different angles and the results are shown in fig. S5. As can be seen, for β ~180º (fig. S5(a)), the withdrawal distances of the sperm are very large, and therefore we can conclude that the CI of sperm with velocities between 40–80 μm/s is very low, and consequently the sperm cannot accumulate nearby the stricture. In addition, when sperm reach the other sidewall, the shear rate at the contact point in the $\hat{n}$ direction is inadequate (0.06–0.054 s^{-1}) to rotate sperm upstream, causing the sperm to move towards the downstream direction. When we decrease β to 130º (fig. S5(b)), the CI starts to increase and accumulation of sperm close to the stricture begins to occur. Sperm with velocities in the range of ~70–80 μm/s can rotate upstream, and therefore

these sperm are the only ones with a chance of passing through the stricture. For a β of 40º (fig. S5(c)), the CIs are very low in comparison with $\beta = 80°$ (Fig. 1 in the main text), and accordingly the chance of sperm to pass through the junction is very low. Moreover, only sperm with velocities in the range of $65 - 80$ μm/s are able to get closer than 5 μm to the stricture (this value is established as the proximity zone in the main text). As the angle decreases to 10º (fig. S5(d)), the CIs are so low that none of the sperm with velocities in the range of 40–80 μm/s are able to enter the proximity zone of the stricture. Unlike the large angles, in this case the shear rate (5.64–6.12 s^{-1}) at the contact points can reorient sperm towards the upstream direction.

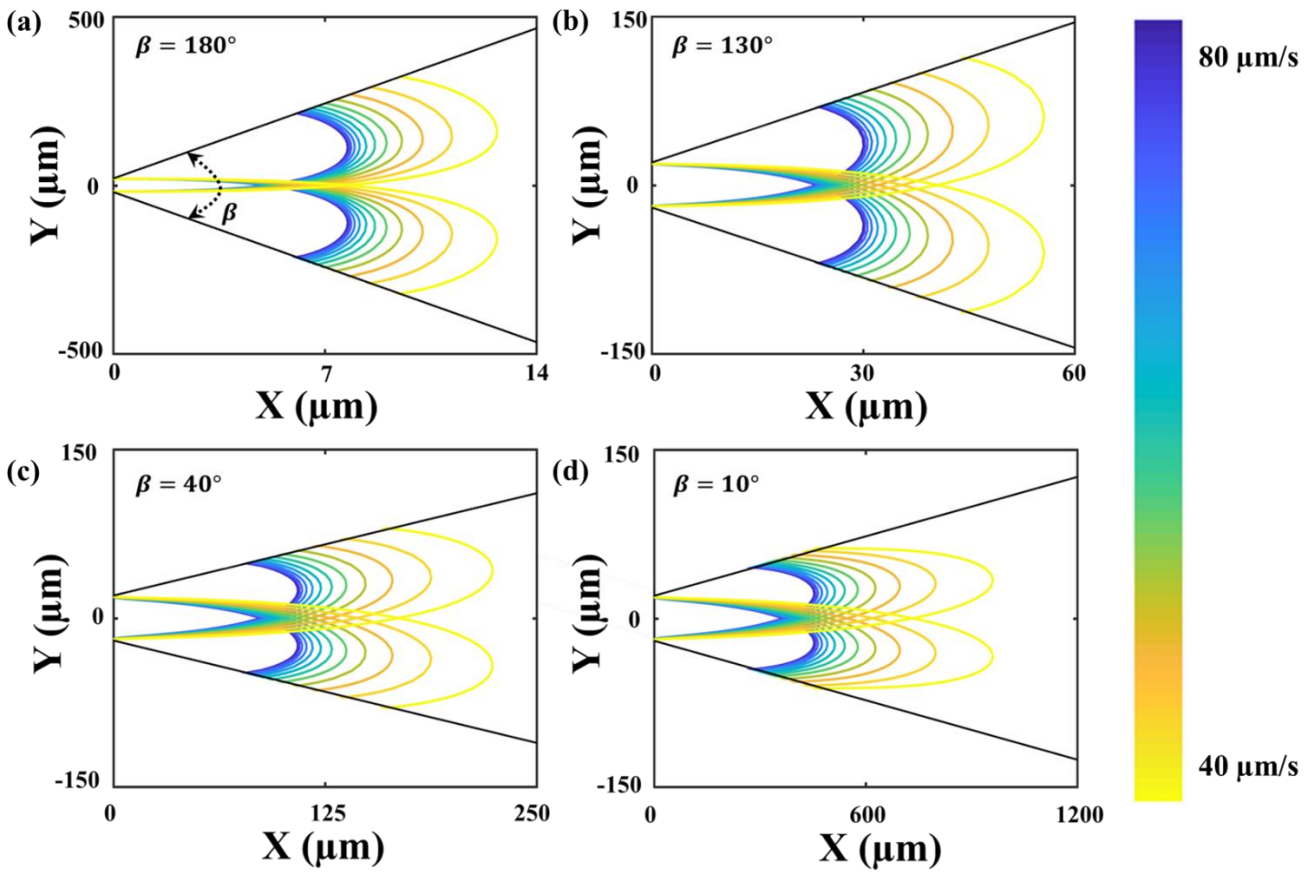

Fig. S5. Impact of stricture mouth angle on the butterfly-shaped motion of sperm. (a) An extremely wide stricture angle (β ~180º) leads to long withdrawal distances and thus low CIs. The low shear rates at the contact points are inadequate to reorient sperm upstream in the stricture direction. (b) Once β is 130º, a few sperm with velocities in the range of ~70–80 µm/s reorient upstream, while the rest of the sperm cannot return to the proximity of the stricture. (c) In acute stricture openings, the shear rate is enough to reorient sperm upstream and the butterfly-shaped motion occurs. However, for β = 40º, only a few sperm with velocities in the range of ~ 65–80 µm/s can get closer than 5 µm to the stricture. (d) At extremely acute angles (β = 10º), long withdrawal distances result. In addition, the proximity condition is satisfied for none of the sperm.

Fokker-Planck equation

The Fokker-Planck equation (Eq. S30) describes the evolution of the probability density function over time(*40*)

$$\frac{\partial P(x,t)}{\partial t} = \frac{\partial}{\partial x}\left(\frac{\partial x}{\partial t}P(x,t) - D_x\left(\frac{\partial P(x,t)}{\partial x}\right)\right) \quad \text{(S30)}$$

in which $P(x,t)dx$ is the likelihood of the sperm location to be between x and $x + dx$, and D_x is the translational diffusion coefficient of the sperm. For large Péclet numbers ($Pe = \frac{\tau_D}{\tau_v} \gg 1$) and the steady state condition ($\frac{\partial P(x,t)}{\partial t} = 0$), Eq. S30 reduces to

$$P(x,t)dx = Cdt. \quad \text{(S31)}$$

Considering the normalization $\int_0^L dxP(x,t) = \int_0^T dtC = 1$, Eq. S31 leads to the probability of the sperm being between x and $x + dx$

$$P(x,t)dx = \frac{dt}{T} \quad \text{(S32)}$$

in which dt is the time elapsed for sperm to swim the distance of dx. Therefore, the probability of the sperm to be closer than a to the stricture is

$$pr\{X \le a\} = \int_0^a dxP(x,t) = \int_0^{T_a}\frac{dt}{T} + \int_{T'_a}^{T}\frac{dt}{T} = \frac{T_a + T - T'_a}{T}. \quad \text{(S33)}$$

in which T_a and T'_a are the corresponding times of $x = a$, in which because of the periodic motion, the sperm pass through this situation twice.

Butterfly-shaped motion in human sperm

The similarity between human and bovine sperm in terms of the shape and swimming mechanism suggests that the motion of human sperm below the stricture is like that of bovine sperm. To experimentally confirm this similarity, we experimentally observed human sperm motion below the stricture (Movie S3). As was expected, we observed the butterfly-shaped swimming path (fig. S6(a)). The withdrawal distances were measured and reported in fig. S6(b). We also observed the human sperm motion in transfer, rotation, and boundary swimming modes (fig. S7(a)). Fig. S7(b) presents the time elapsed in these modes.

The data extracted for the human sperm (fig. S6 and S7) confirms the similarity in the data trends between the human and bovine sperm. However, the slower swimming speed of human sperm led to longer periods and withdrawal distances. Moreover, for very slow sperm ($v < 35$ μm/s) the time required for the transfer mode was longer than the time required for a sperm to completely reorient itself upstream, and thus the reorientation happens below reaching the other sidewall, preventing transfer to the other sidewall. This leads to slow sperm appearing to be static in the observer frame. In fact, once their swimming direction is completely aligned with the flow streamlines, their propulsive force is neutralized by the fluid flow, as can be seen in Movie S3.

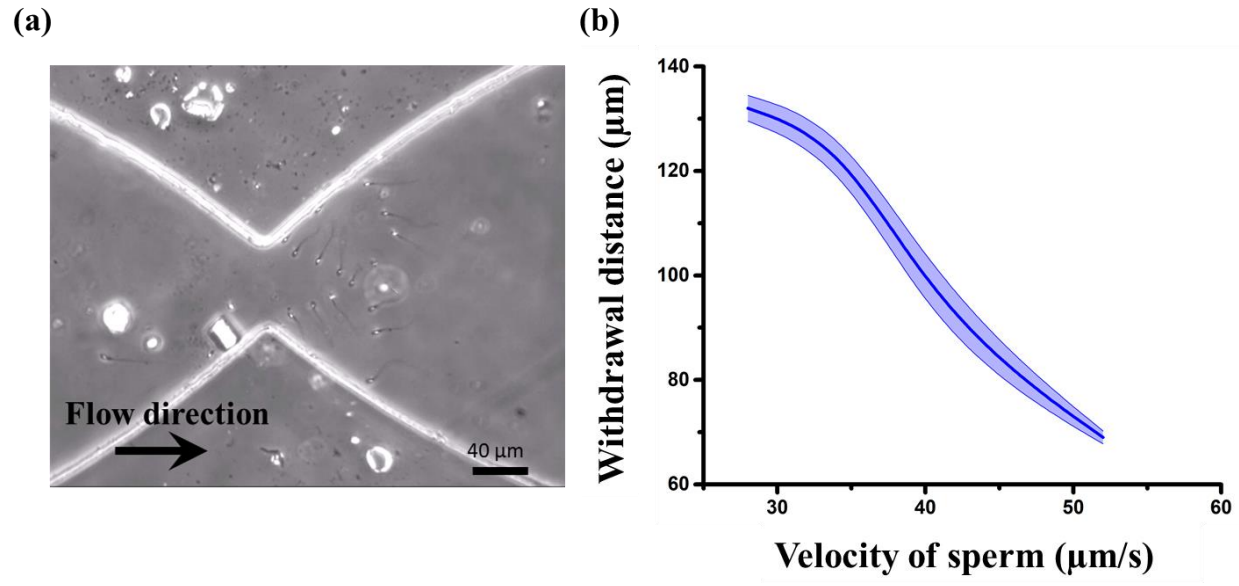

Fig. S6. Butterfly-shaped motion of human sperm. (a) Human sperm swim on a butterfly-shaped path and the total swimming direction is counter to the flow. (b) The withdrawal distance was extracted for different sperm with different velocities.

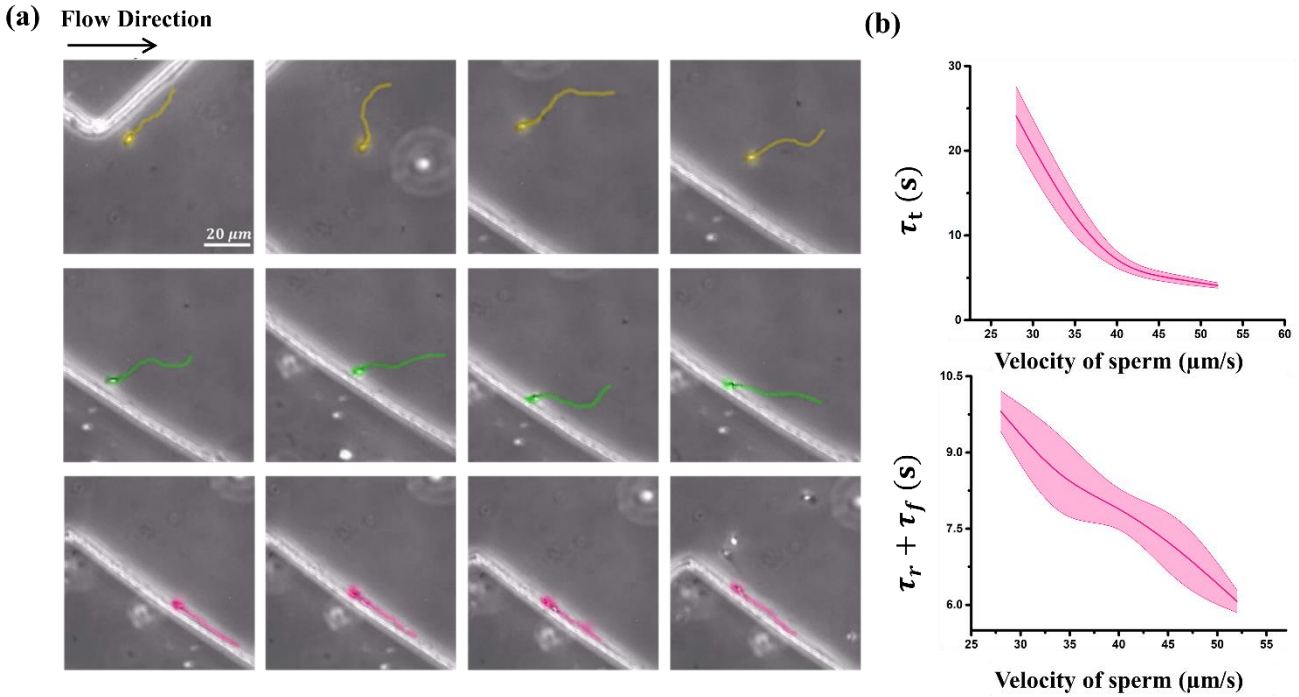

Fig. S7. Transfer, rotation, and boundary swimming modes with corresponding times for human sperm. (a) The sperm swimming in the transfer, rotation, and boundary swimming modes are illustrated in the first, second, and third rows, respectively. To visualize the sperm in each frame, three colors are used. The scale bar and flow direction are the same for all pictures. (b) The time elapsed in the transfer (τ_t) and combined rotation and boundary swimming modes ($\tau_{r+}\tau_f$) .

Characterization of the stricture's gate-like behavior

The sperm moving below the stricture pass through it depending on the shear rate within the stricture, as can be seen in Movie S5. To characterize the gate-like role of the stricture in motility-based selection of sperm, we changed the flow rate systematically and decreased it in a linear manner, causing the shear rate within the stricture to decay. The velocity of the sperm that passed the barrier (i.e., the threshold sperm velocity) with regards to the shear rate of the stricture is shown in fig. S8. To maximize the precision of our measurements, we measured the velocity of sperm once the swimmer reached the region of the channel with minimum medium velocity field. As can be seen in fig. S8, there is a linear correlation between the threshold sperm velocity and the shear rate in the stricture, which we repeated in three different experiments with different samples. Moreover, we performed a Pearson correlation test to examine the linear correlation. The obtained correlation coefficient was equivalent to 0.959 with a p-value of less than 0.01. This p-value indicates a significant linear correlation between the shear rate of the stricture and the threshold sperm velocity.

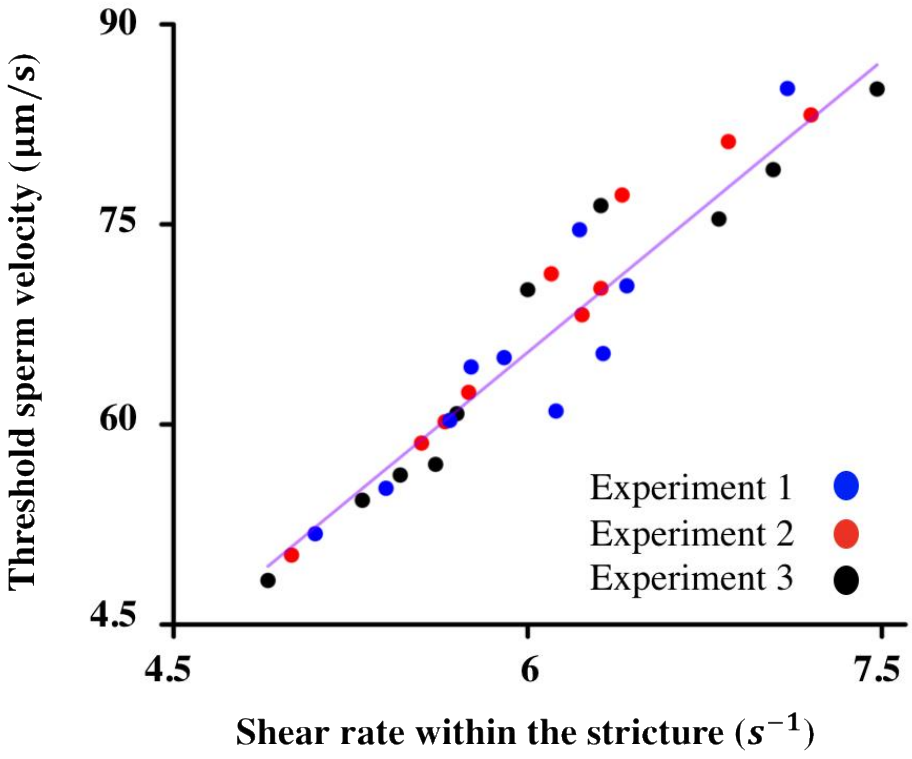

Fig. S8. Threshold sperm velocity versus shear rate of the stricture.